



NUMERICAL SIMULATIONS OF FLOW PAST AN AUTONOMOUS UNDERWATER VEHICLE AT VARIOUS DRIFT ANGLES

Sreekar Gomatam¹, S. Vengadesan², S. K. Bhattacharyya³

¹Research Scholar, Department of Applied Mechanics, Indian Institute of Technology-Madras, Chennai-600036, India, Email: sreekargomatam@gmail.com

²Associate Professor, Department of Applied Mechanics, Indian Institute of Technology-Madras, Chennai-600036, India, Email: vengades@iitm.ac.in

³Professor, Department of Ocean Engineering, Indian Institute of Technology-Madras, Chennai-600036, India, Email: skbh@iitm.ac.in

Abstract:

Three dimensional (3D) flow past an Autonomous Underwater Vehicle (AUV) is simulated using a Computational Fluid Dynamics (CFD) approach at a Reynolds (Re) number of 2.09×10^6 . A non-linear $k-\varepsilon$ (NLKE) turbulence model is used for solving the Reynolds Averaged Navier-Stokes equations (RANSE). The effect of control surfaces over the flow, the flow interaction between hull and appendages at various Angles of Attack (AoA) and the effect of the symmetry plane is studied. Flow structure, variation of flow variables and force distribution for various AoA are presented and discussed in detail.

Keywords: AUV, CFD, turbulence model, Angle of Attack, non-linear $k-\varepsilon$ model, RANSE

NOMENCLATURE:

U_i	Velocity in i^{th} direction	U_∞	Free stream velocity
ρ	Density of water	U	Velocity vector
k	Turbulent kinetic energy	R	Radial distance of a point from vehicle surface
ε	Turbulent dissipation rate	R_0	Radius of the hull
ν_t	Turbulent viscosity	R_{max}	Maximum radius of the hull
S_{ij}	Mean strain rate	S	Projected planform area of the vehicle
C_D	Mean drag coefficient	A	Projected frontal area of vehicle
C_L	Mean lift coefficient	L	Length of the vehicle

1. Introduction

Predicting the hydrodynamic coefficients of an AUV in the design phase is very important to understand the maneuvering performance of the vehicle. Methods for predicting these hydrodynamic coefficients for a fully submerged vehicle can be dated back to the methods developed for aero planes, which were modified for missiles, then for torpedoes and subsequently adopted for submarines and AUVs. Use of experimental techniques to design and develop the trajectory of an AUV is time consuming, expensive and requires sophisticated instrumentations. Predictive methods can be used to determine the location and shape of the control surfaces and the propeller. These methods include the Analytical and Semi-empirical (ASE) methods, which are developed in the aerospace industry and then adopted for streamlined underwater vehicles. Predictive methods, such as the approach presented by the DATCOM (Finck, 1978), can yield reasonable results if the geometry of the vehicle is not too complex. Another method to predict the external forces on the vehicle is to use the component built-up method. In this method, hydrodynamic forces are derived from empirical relations that only require the specifications of the geometry of the component. Each component of the vehicle, such as hull, control surfaces and thrusters, is modeled separately using simple hydrodynamic relations. The forces and moments from each component are then summed to provide the total forces and moments acting on the vehicle. Researchers who used component built-up method in their AUV simulations include Nahon (1996), Prestero (2001), and Perrault *et al* (2003). Though this method can predict the hydrodynamic forces at small angles of

attack, the method failed to address the non-linear flow behavior and the cross flow currents that develop at high angles of attack. Newman (1992) and Sahin *et al* (1997) used panel methods to predict the hydrodynamic coefficients of submerged vehicles. This method is based on potential flow theory and it fail to predict the forces and moments at high incidence angles and in the presence of cross currents. Moreover, the interactions between hull and control surfaces are not well addressed. A surge in low cost, high performance computing resulted in the increased application of RANSE based CFD techniques to predict the hydrodynamic coefficients. Sarkar *et al* (1997) evaluated the performance of different models of the $k-\epsilon$ family in predicting the hydrodynamic coefficients for various axisymmetric hull forms (AFTERBODY 1, AFTERBODY 2, MODIFIED SPHERIOD and F-57). Jagadeesh and Murali (2005) studied the performance of low-Re turbulence models in predicting the forces and moments for different streamlined hull forms. The application and performance of Large Eddy Simulation (LES) and Detached Eddy Simulation (DES) for flow past submarines and AUVs was studied by Alin *et al* (2010). They studied the LES and DES performance for DARPA Suboff configurations (bare hull and fully appended). Barros *et al* (2008 a, b) studied the flow past an axisymmetric barehull at different incidence angles using standard models for turbulence closure. Recently, Sakthivel *et al* (2011) applied a non-linear $k-\epsilon$ model to study flow characteristics and variation of flow variables, forces at different incidence angles for a Myring type, axisymmetric barehull. Details of flow simulations for fully appended AUV at different incidence angles using RANSE based CFD are rather scarce. The objective of this paper is to address this issue.

2. Governing Equations

Three dimensional Reynolds Averaged Navier-Stokes (RANS) equation for an incompressible flow along with the continuity equation are given below

$$\frac{\partial U_i}{\partial t} + \frac{\partial U_j U_i}{\partial x_j} = -\frac{1}{\rho} \frac{\partial p}{\partial x_i} + \frac{\partial(-\overline{u'_i u'_j})}{\partial x_j} + \nu \frac{\partial^2 U_i}{\partial x_j x_j} \tag{1}$$

$$\frac{\partial U_i}{\partial x_i} = 0 \tag{2}$$

where, U_i is the mean velocity in the i^{th} direction, ρ is the density of the fluid and $\overline{u'_i u'_j}$ is the Reynolds stress.

This Reynolds stress is modeled using a $k-\epsilon$ turbulence model. The transport equations for turbulent kinetic energy (k) and the turbulent energy dissipation rate (ϵ) in a standard $k-\epsilon$ model are given by

$$\frac{Dk}{Dt} = -\overline{u'_i u'_j} \frac{\partial U_i}{\partial x_j} - \epsilon + \frac{\partial}{\partial x_j} \left\{ \left(\frac{\nu_t}{\sigma_k} + \nu \right) \frac{\partial k}{\partial x_j} \right\} \tag{3}$$

$$\frac{D\epsilon}{Dt} = -C_{\epsilon 1} \frac{\epsilon}{k} \overline{u'_i u'_j} \frac{\partial U_i}{\partial x_j} - C_{\epsilon 2} \frac{\epsilon^2}{k} + \frac{\partial}{\partial x_j} \left\{ \left(\frac{\nu_t}{\sigma_\epsilon} + \nu \right) \frac{\partial \epsilon}{\partial x_j} \right\} \tag{4}$$

where, $C_{\epsilon 1}$ and $C_{\epsilon 2}$ are constants, σ_k and σ_ϵ are the turbulent Prandtl number for k and ϵ respectively. In a standard $k-\epsilon$ model, Reynolds stress is related to the strain rate in a linear fashion as given by Boussinesq approximation given below

$$-\overline{u'_i u'_j} = \nu_t S_{ij} - \frac{2}{3} k \delta_{ij} \tag{5}$$

But, this model does not include the anisotropy of turbulence. This deficiency is addressed by including non-linear terms in the Reynolds stress constitutive relation as given below

$$-\overline{u'_i u'_j} = \nu_t S_{ij} - \frac{2}{3} k \delta_{ij} - \frac{k}{\epsilon} \nu_t \sum_{\beta=1}^3 C_\beta (S_{\beta ij} - \frac{1}{3} S_{\beta\alpha\alpha} \delta_{ij}) \tag{6}$$

$$S_{1ij} = \frac{\partial U_i}{\partial x_j} \frac{\partial U_j}{\partial x_i}; S_{2ij} = \frac{1}{2} \left(\frac{\partial U_j}{\partial x_i} \frac{\partial U_i}{\partial x_j} + \frac{\partial U_j}{\partial x_j} \frac{\partial U_i}{\partial x_i} \right); S_{3ij} = \frac{\partial U_j}{\partial x_i} \frac{\partial U_i}{\partial x_j} \tag{7}$$

ν_t is the eddy viscosity, S_{ij} is the mean strain rate tensor and δ_{ij} is Kronecker delta function. The non-linear terms in the above equation are reported in Kimura and Hosoda (2003) and validated for different complex flows. The model coefficients in the transport equation are tuned to satisfy the realizability inequalities for the three dimensional flow field. This non-linear $k-\epsilon$ (NLKE) model is incorporated in Fluent[®] through User Defined Functions (UDF). The implementation of this UDF was earlier validated for flow past a square cylinder (Ramesh *et al*, 2006) and flow past a circular cylinder (Ayyappan and Vengadesan, 2008). In addition, the implementation of this UDF for underwater vehicles was validated by Sakthivel *et al*, (2011) by studying flow past a barehull at different drift angles of the vehicle.

3. Numerical Methodology

MAYA, an AUV developed by National Institute of Oceanography (NIO), Goa, under a joint Indo-Portuguese program is selected to carry out the current study. It is a Myring type body with a nose section, a

cylindrical middle section and a tail section. The nose and tail section are defined as a modified semi-elliptical distribution and a cubic spline distribution respectively (Myring, 1976). The three control surfaces are NACA 0015 airfoils. Two are in the stern plane (CS1, CS3) and one in the bottom rudder (CS2) plane. A schematic of the barehull, a control surface and the appended vehicle is shown in Fig. 1 and the geometric specifications are provided in Table 1. Though the appended vehicle is not axisymmetric, starboard-port symmetry exists.

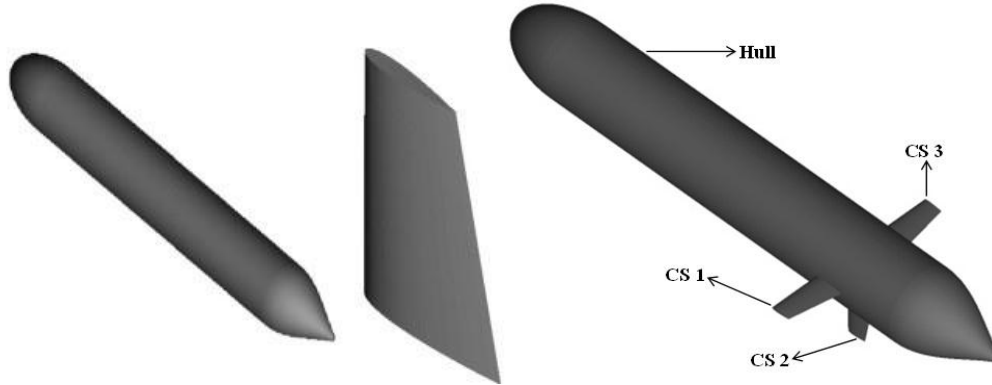


Fig. 1: Isometric views of bare hull, control surface and MAYA

Table 1: Major geometric properties of maya, bare hull and control surface

BAREHULL		CONTROL SURFACE	
Hull length (L)	1.742m	Single foil span	0.16m
Maximum hull diameter	0.234m	Root chord	0.09m
Middle body length	1.246m	Tail chord	0.06m
Nose length	0.217m	Thickness chord	0.15
Myring body parameter	25 ⁰	Aspect ratio	4.26

Detailed domain and grid independence tests are carried out initially to determine an optimum domain and grid size for further computations. The initially selected domain size, Domain 1, is same as that is specified in Sakthivel *et al.*, (2011), which was determined after a detailed validation and domain independence study for the barehull. The details of the various domain sizes and the corresponding drag coefficients are provided in Table 2. Grid independence tests are then performed to determine an optimum grid density for the selected domain. The details of the grid independence tests are provided in Table 3.

Table 2: Details of domain independence tests

	Domain dimension (Streamwise (X) x Cross-stream (Y) x Spanwise (Z) directions)	Drag Force (N)	Drag coefficient
Domain 1	6.2L * 0.78L * 0.78L	16.111	0.464
Domain 2	6.2L * 1.18L * 1.18L	17.597	0.505
Domain 3	6.4L * 1.38L * 1.38L	17.922	0.511
Domain 4	6.4L * 1.58L * 1.58L	17.993	0.513

Table 3: Details of grid independence tests

	Grid size	Drag coefficient
Grid A	96 * 42 * 42	0.511
Grid B	140 * 42 * 42	0.458
Grid C	190 * 34 * 34	0.410
Grid D	190 * 42 * 42	0.407

From the domain independence tests, it can be observed that the variation in the drag coefficient for Domain 2 and Domain 3 is very small. In order to have enough space for flow development during the angle of attack studies, Domain 3 is selected for further studies though it is computationally expensive when compared to Domain 2. An initial grid of 96 * 42 * 42 nodes is selected from Sakthivel *et al.* (2011). Grid independence tests are then performed by varying the grid density by 10% initially in the streamwise direction and then in the cross-stream and spanwise direction simultaneously. The variation in the drag coefficient between Grid C and

Grid D is very small. Hence, Grid C is selected as the optimum grid size. Thus, for all further studies, a domain of size $6.4L * 1.38L * 1.38L$ is selected. A schematic of the selected domain is shown in Fig. 2. A body fitted H-grid is used for meshing. A typical 3D computational mesh is shown in Fig. 3. Front view of the domain in the XY plane with the mesh and an enlarged view of the mesh around the vehicle in the same plane are shown in Fig. 4.

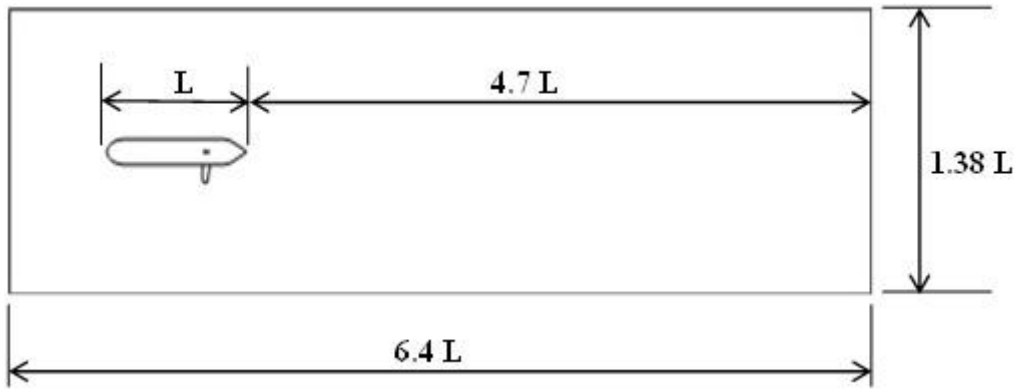


Fig. 2: Schematic of the computational domain

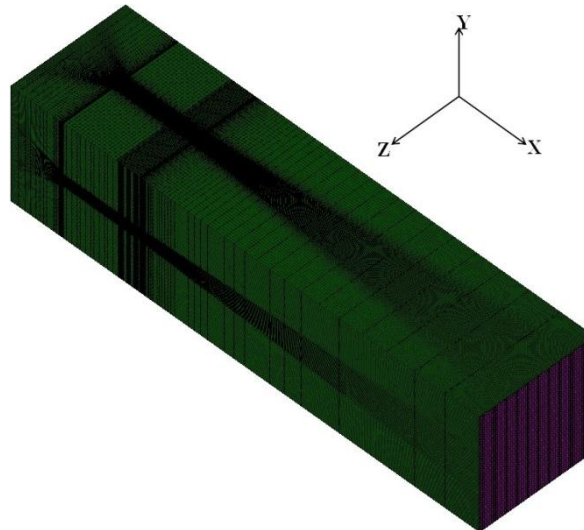


Fig. 3: 3D computational mesh over MAYA

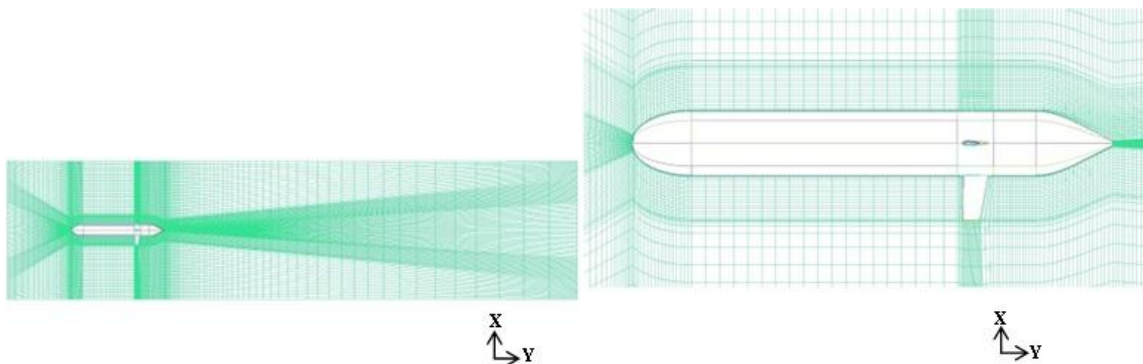


Fig. 4: Left) Mesh in front view at $Z=0$ and Right) Zoomed view around the vehicle

Drag force from current simulations using non-linear $k-\epsilon$ model (NLKE) and the experimental data from tow tank experiments (Madhan *et al*, 2006) are compared in Fig. 5. From Fig. 5, it can be observed that the drag force predicted by the non-linear $k-\epsilon$ model for a fully appended vehicle is matching well with that of experimental results.

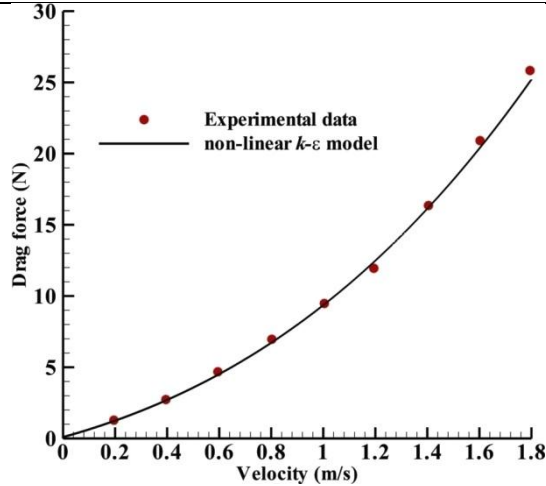


Fig. 5: Comparison of drag force between experiments and simulations

To perform the angle of attack studies, the computational domain is placed in a much larger domain referred as “Outer domain” and the initial domain is referred to as “Base domain”. Then the base domain is rotated in the outer domain to achieve the required drift angle of the vehicle. The boundary conditions are imposed on the outer domain and the flow variables are monitored in the base domain as it is the region of interest. Front view of the outer domain for 20^0 angle of attack over Z-axis and the domain sizes are shown in Fig. 6. The boundary conditions imposed are as follows:

1. Face AC is set as velocity inlet. Along with this, the turbulent intensity and the turbulent length scale are specified. Turbulent intensity is set to 0.5% and the length scale is $0.001L$. (Sarkar *et al*, 1997).
2. Face BD is set to outflow condition, i.e. the flow gradients normal to the boundary are set to zero.
3. The faces AB, CD are set to symmetry.
4. No slip condition is imposed on the barehull and control surfaces of MAYA.

Commercial software package, FLUENT® 13.0, on an AMD Opteron™ 6170 (Processing speed of 2.1 GHz) is used for the simulations. SIMPLE algorithm is used for pressure-velocity coupling. Second order upwinding scheme is used for discretizing the momentum, turbulent energy and dissipation equations. The convergence criterion is set to 10^{-4} for all the equations. A time step of 5×10^{-4} s is used. The standard k-ε and the non-linear k-ε models are high Re models. They use the wall functions to calculate the flow variables near the wall. To capture the flow features near the wall, a y^+ value between 30 and 80 is required. This is achieved by placing the first grid point 0.003m from the vehicle. This corresponds to a y^+ value of 40. All simulations are performed at an incoming flow velocity of 1.2m/s and the corresponding Re based on the length of the vehicle is 2.09×10^6 .

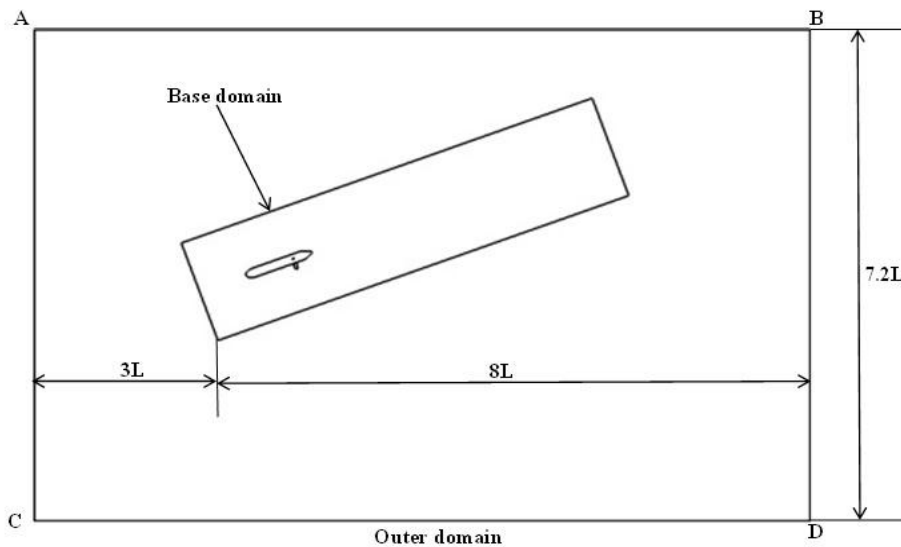


Fig. 6: Front view of Outer and Base domain for an AoA of 20^0

4. Results and Discussion

The flow is simulated for six flow through times. One flow through time can be defined as the time taken for a fluid particle to travel from the inlet to the outlet of the domain. Based on the domain size, one flow through time is equivalent to 16s. Then the flow variables of interest, i.e., pressure and velocity are time-averaged over two flow through time. Summarizing, for all the angles of attack, the flow is simulated for 100s and the flow variables at the end of 100s are considered. The results presented are for various angles of attack of the vehicle over Z-axis and Y-axis.

4.1 Force coefficients

Drag and lift force provide an insight into the pressure distribution around the vehicle. Drag force, lift force and their corresponding coefficients for different Angles of Attack over Y and Z axes are presented in Table 4.

Table 4: Variation of drag, lift force and the corresponding coefficients with AoA

		Z-Axis (α)					Y-Axis (β)				
		-20 ⁰	-10 ⁰	0 ⁰	10 ⁰	20 ⁰	-20 ⁰	-10 ⁰	0 ⁰	10 ⁰	20 ⁰
Drag	Pressure (N)	25.72	12.25	7.89	12.19	25.45	18.28	9.74	7.89	9.71	18.28
	Viscous (N)	4.28	4.00	4.05	4.10	4.27	4.37	4.08	4.05	4.07	4.37
	Total (N)	30.00	16.25	11.95	16.29	29.72	22.65	13.82	11.95	13.78	22.65
	C _D	0.86	0.47	0.34	0.47	0.85	0.65	0.4	0.34	0.39	0.65
Lift	Pressure (N)	55.08	26.67	0.16	-26.33	-54.29	5.98	2.24	0.16	2.23	6.0
	Viscous (N)	-0.25	-0.11	0	0.12	0.26	0.1	0.004	0	0.005	0.1
	Total (N)	54.83	26.56	0.16	-26.11	-54.03	5.99	2.224	0.16	2.235	6.1
	C _L	1.57	0.76	0.01	-0.75	-1.55	0.17	0.06	0.01	0.06	0.17

C_D and C_L are defined as follows

$$C_D = \frac{F_D}{\frac{1}{2} U_\infty^2 S} \quad C_L = \frac{F_L}{\frac{1}{2} U_\infty^2 A}$$

where, U_∞ is the reference velocity, S is the projected frontal area of the vehicle and A is the projected planform area of the vehicle.

Variation of C_D with C_L is plotted in Fig. 7 and the details are provided in Table 4. From Table 4, it is observed that the viscous drag or the skin-friction drag almost remains constant over the entire range of α and β . The main contribution to the forces is from the pressure variation. As the Angle of Attack (AoA) is increased, the pressure drag also increases and it can be inferred that the pressure gradients around the vehicle are high, resulting in such large values of drag. For an angle of attack over Z-axis, at -20⁰ and 20⁰, pressure drag contributes more than 72% of the total drag and this value is almost 250% more than the pressure drag value at 0⁰ angle of attack. But, for an angle of attack over the Y-axis, the total drag values are much less when compared to the corresponding values of angle of attack over Z-axis. Irrespective of the angle of attack or the axis, the main component of the drag force is the pressure drag which is caused by the pressure gradients around the vehicle. When comparing the lift forces, it can be observed that the total lift force generated for an angle of attack over the Y-axis is very small when compared to the angle of attack over the Z-axis. Over the entire range of the angle of attack over the Y-axis, the lift value is always positive, unlike for an angle of attack over the Z-axis. This variation results in a parabolic curve for an AoA over Z-axis and a straight line for an AoA over Y-axis as shown in Fig. 7. Also, it can be inferred that the direction and the magnitude of the angle of attack of the flow results in different flow patterns around the vehicle. Because of the angle of attack and the loss in axisymmetry of the vehicle due to the presence of control surfaces, large force variation is observed which is due to the

pressure gradients around the vehicle. When compared to a bare hull (Sakthivel *et al*, 2011), the values of lift and drag for the same angle of attack, regardless of the axis, are very high.

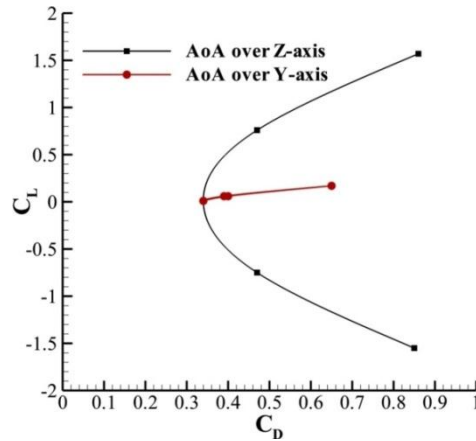


Fig. 7: Variation of C_L with C_D

From Table 4, it is observed that the force variation for -20° and 20° or -10° and 10° is almost the same for both Z-axis and Y-axis angle of attack. For better understanding the variation of the forces, the drag force acting on the hull and the control surfaces for a typical angle of attack are tabulated separately in the following table.

Table 5: Drag force variation for 20° and -20° AoA over Y, Z axes

	$\beta=20^\circ$			$\beta=-20^\circ$			$\alpha=20^\circ$			$\alpha=-20^\circ$		
	P (N)	V (N)	T (N)	P (N)	V (N)	T (N)	P (N)	V (N)	T (N)	P (N)	V (N)	T (N)
Hull	13.639	4.045	17.684	13.563	4.044	17.607	17.393	4.029	21.422	18.093	4.131	22.224
CS 1	0.727	0.125	0.852	0.327	0.130	0.457	3.533	0.077	3.61	3.663	0.079	3.742
CS 2	3.603	0.073	3.676	3.638	0.073	3.711	1.064	0.085	1.149	0.521	0.086	0.607
CS 3	0.321	0.13	0.451	0.750	0.125	0.875	3.491	0.075	3.566	3.520	0.078	3.598
Total	18.280	4.373	22.653	18.278	4.372	22.65	25.481	4.266	29.747	25.78	4.374	30.154

P = Pressure drag; V = Viscous drag; T = Total drag

From Table 5, it is observed that for an angle of attack over Z-Axis (α), the drag force acting on the hull, the control surfaces on the starboard (CS3) and on the port (CS1) is almost same. But the drag force acting on the rudder control surface (CS2) is varying which is because of the angle of attack. Though the drag force is same, depending on the angle of attack over Z-axis, the lift force acting on the vehicle is different as can be observed from Table 4. For an angle of attack over the Y-axis (β), the forces acting on the hull and CS2 are same. But, the drag force acting on CS1 for $\beta=20^\circ$ is same as the force acting on CS3 for $\beta=-20^\circ$ and vice-versa. This results in the total drag for the entire AUV remaining the same for $\alpha=20^\circ$ and $\alpha=-20^\circ$ as well as for $\beta=20^\circ$ and $\beta=-20^\circ$.

4.2 Streamline patterns

To understand the flow phenomena better, streamlines at different sections along the length of the vehicle in planes perpendicular to the streamwise direction (X-axis) for different angles of attack are plotted in Figs. 8 to 11. The x/L locations considered are:

- a) $x/L=0.062$, the middle section of the nose
- b) $x/L=0.5$, the mid-section of the vehicle
- c) $x/L=0.69$, 0.1m before the leading edge of the control surfaces
- d) $x/L=0.74$, 0.1m after the trailing edge of the control surfaces
- e) $x/L=0.84$, the start of the tail section
- f) $x/L=0.93$, mid-section of tail.

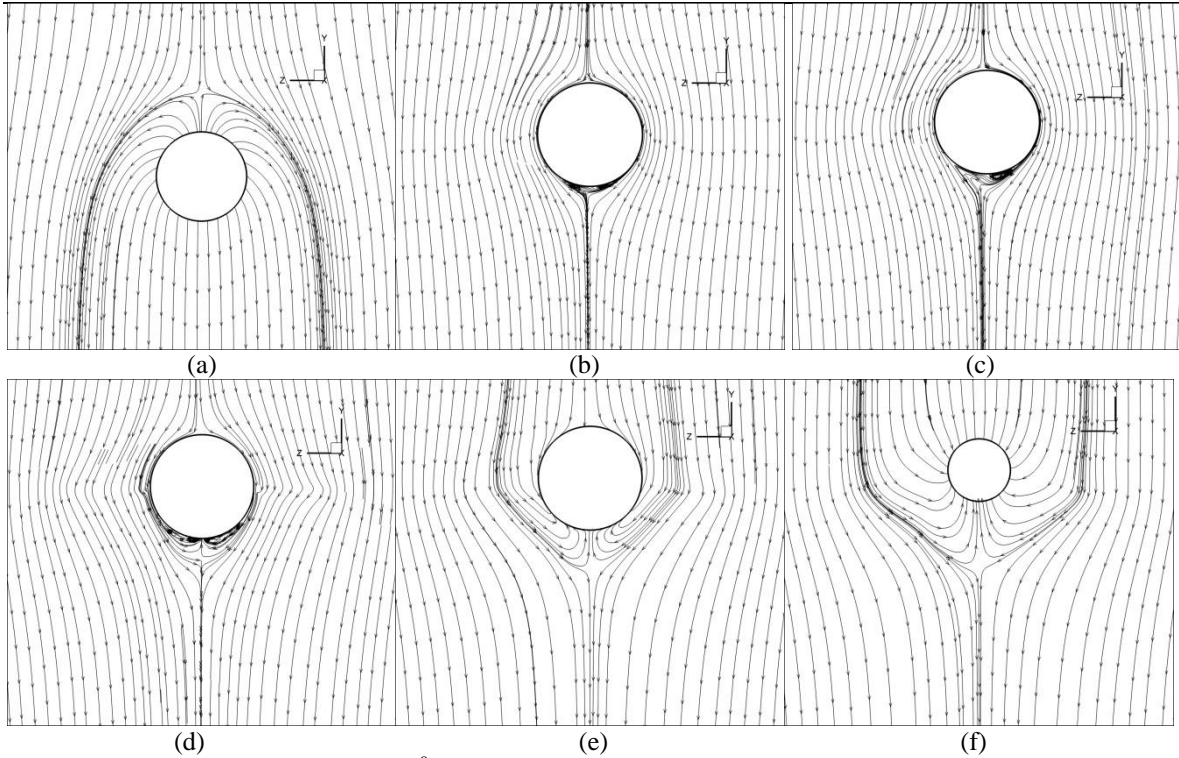


Fig. 8: Streamline patterns for $\alpha=10^\circ$ at $x/L=$ (a) 0.062, (b) 0.5, (c) 0.69, (d) 0.74, (e) 0.84 and (f) 0.93 respectively

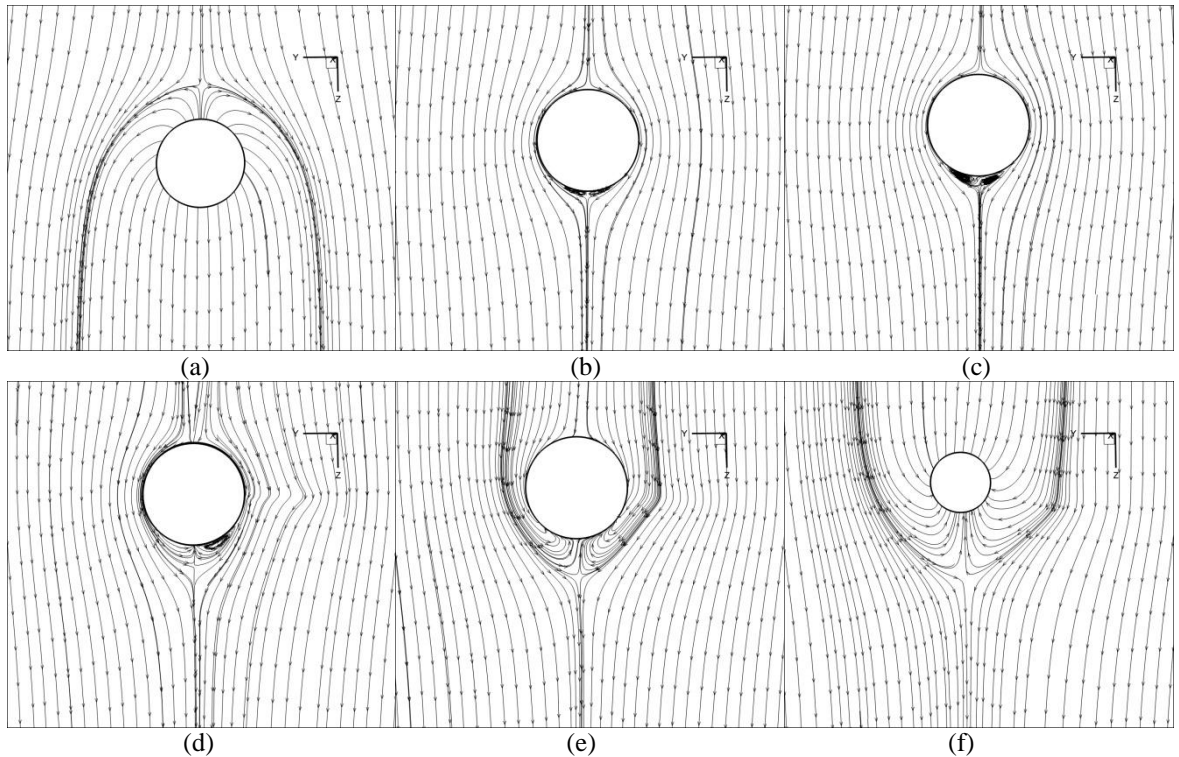


Fig. 9: Streamline patterns for $\beta=10^\circ$ at $x/L=$ (a) 0.062, (b) 0.5, (c) 0.69, (d) 0.74, (e) 0.84 and (f) 0.93 respectively

These sections correspond to locations where there is a continuous change in the geometry or where the flow features are expected to vary sharply. The same x/L locations are considered for both α and β . In Fig. 8, the streamline patterns at different x/L locations for an AoA of 10° over Z-axis are plotted and in Fig. 9, streamlines

at the same x/L locations for a 10° AoA over Y-axis are plotted. The flow is completely separated from the vehicle at $x/L=0.062$ as is observed in both Figs. 8a and 9a. Flow re-attaches to the vehicle somewhere between $x/L=0.062$ and 0.5. Formation of a pair of vortices on the bottom side of the vehicle is observed at $x/L=0.5$ for both α and β (Fig. 8b and 9b). Till here, the flow pattern is almost the same for both $\alpha=10^\circ$ and $\beta=10^\circ$. At $x/L=0.69$, the effect of control surfaces is observed. At $x/L=0.69$, due to the effect of control surface (CS2) in the rudder plane, the vortex pair grows in strength for $\alpha=10^\circ$ when compared to the flow at the same location for $\beta=10^\circ$ (Figs. 8c, 9c). For $\beta=10^\circ$, at $x/L=0.74$, the effect of control surface in the stern plane influences the flow depending on the angle of attack. As the flow proceeds further downstream, the vortices expand and the flow separates from the vehicle. Thus, over the entire length of the vehicle, the flow is initially separated from the vehicle due to the geometry and the angle of attack. As the flow proceeds downstream, the flow is attached to the vehicle. But due to the presence of the control surfaces, the continuous change in the geometry of the tail section, the flow separates again from the vehicle (Figs. 8e, 8f, 9e and 9f).

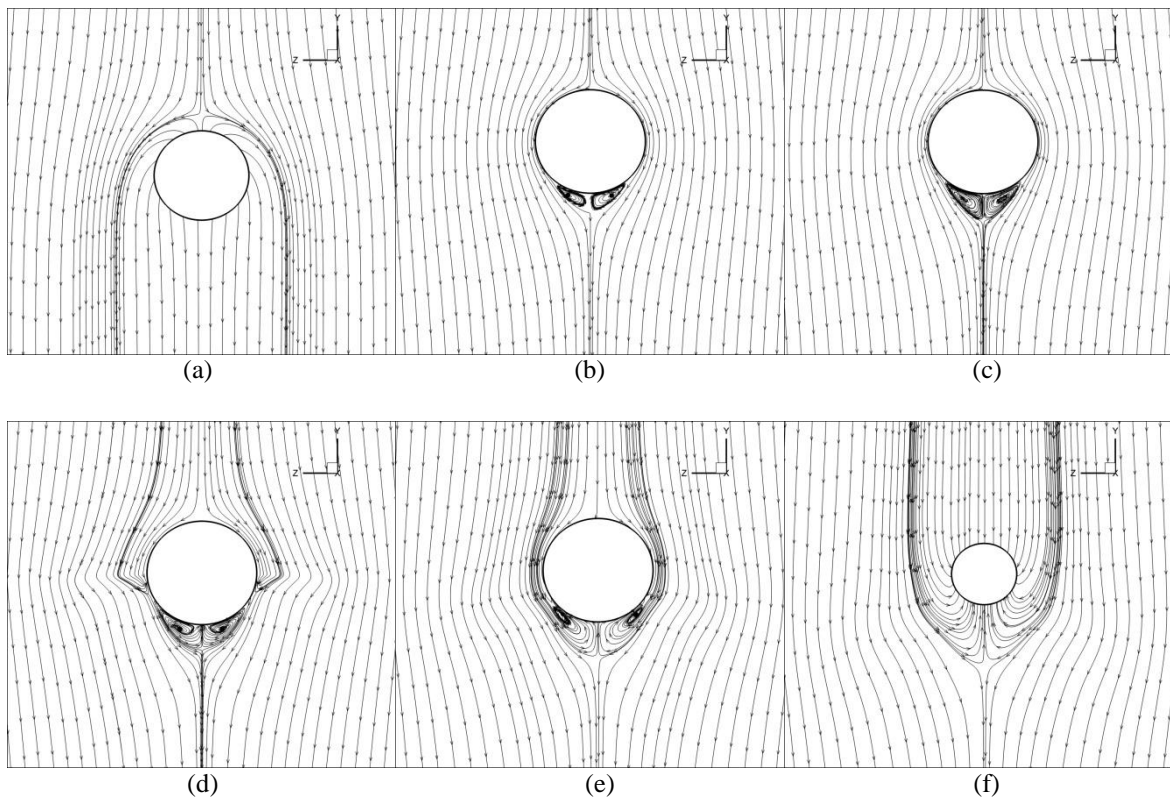


Fig. 10: Streamline patterns for $\alpha=20^\circ$ at $x/L=$ (a) 0.062, (b) 0.5, (c) 0.69, (d) 0.74, (e) 0.84 and (f) 0.93 respectively

Streamlines plotted at different x/L locations for an angle of attack of 20° are presented in Figs. 10 and 11. Comparing the streamlines in Figs. 10 and 11, it can be observed that the flow pattern is the same for $x/L=0.062$ and 0.5. When compared to the 10° AoA, the size of the vortex pair is higher for higher angle of attack (compare to Figs. 8b and 10b or 9b and 11b). At $x/L=0.74$, the trailing edge of the control surface, for $\alpha=20^\circ$, the flow pattern on either side of the XY plane is the same. But for $\beta=20^\circ$, the control surface on the right half (CS3) influences the flow more than CS1. Downstream of the trailing edge of the control surfaces, i.e., at $x/L=0.84$, the vortex pair on the bottom side of the vehicle stretches and the flow just starts to separate from the vehicle unlike for a 10° AoA, for which the flow is completely separated from the vehicle at the same streamwise location. Observing the streamline patterns plotted at different x/L locations, it can be concluded that the three dimensional flow is not just because of the angle of attack alone, but because of a combined effect of the control surfaces and the angle of attack.

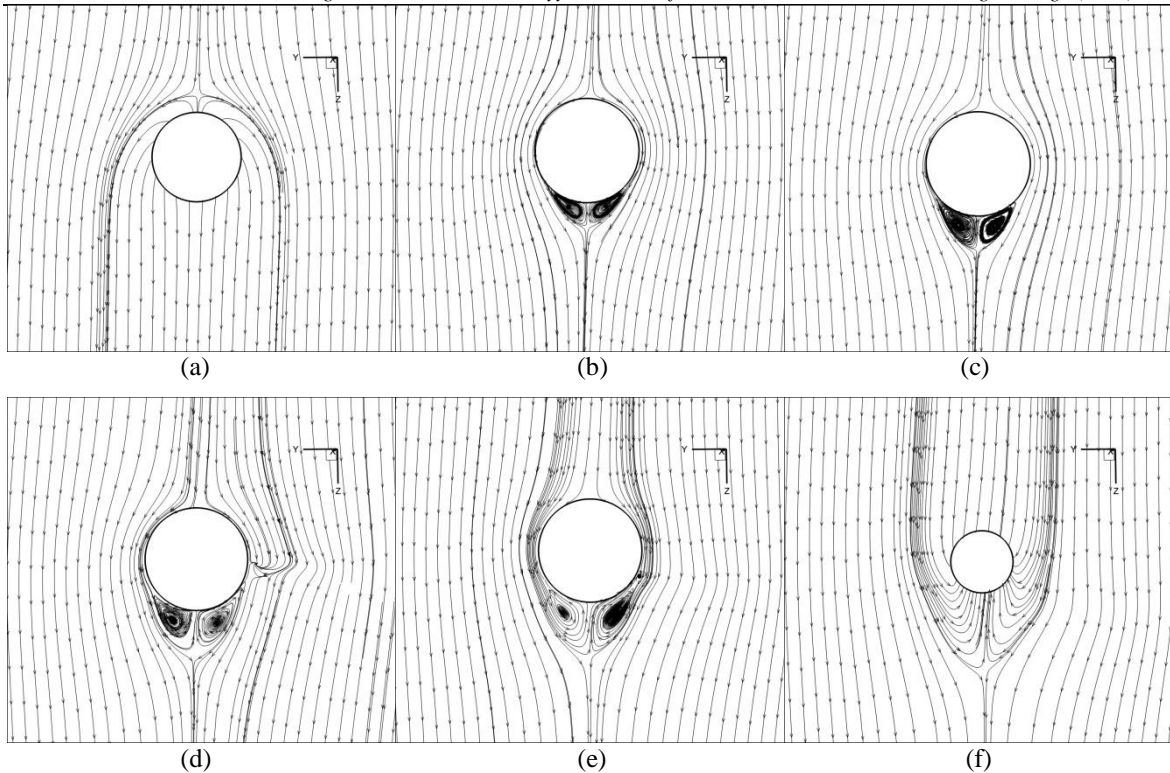


Fig. 11: Streamline patterns for $\beta=20^\circ$ at $x/L=$ (a) 0.062, (b) 0.5, (c) 0.69, (d) 0.74, (e) 0.84 and (f) 0.93 respectively

4.3 Surface pressure distribution

To understand the flow features in a quantitative way, surface pressure variation around the circumference of the vehicle at different x/L values for different angles of attack are plotted. The nomenclature for the azimuthal angle, θ as seen from the front end of the vehicle is shown in Fig. 12. Two control surfaces are in the Z-axis (stern plane), at $\theta=90^\circ$ and $\theta=270^\circ$ and one in the bottom Y-axis (rudder plane) at $\theta=180^\circ$.

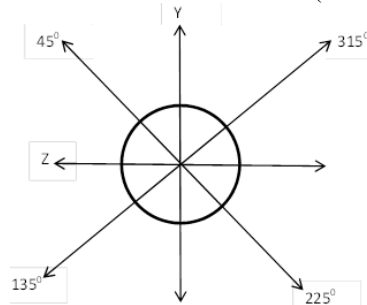


Fig 12: Nomenclature for the azimuthal angle (θ) around the vehicle

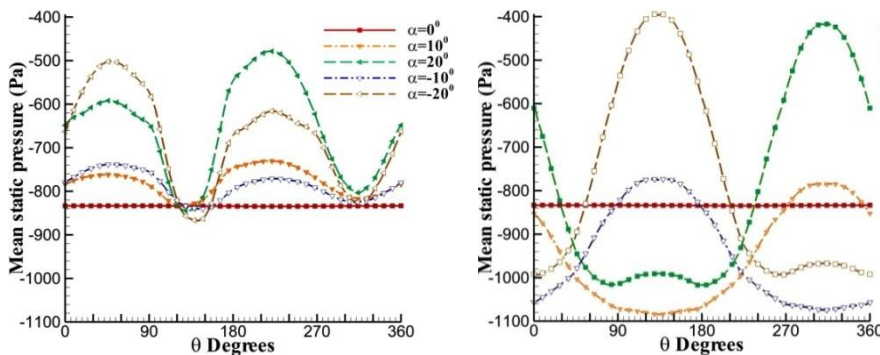


Fig. 13: Variation of mean static pressure at $x/L=0.5$ for different AoA

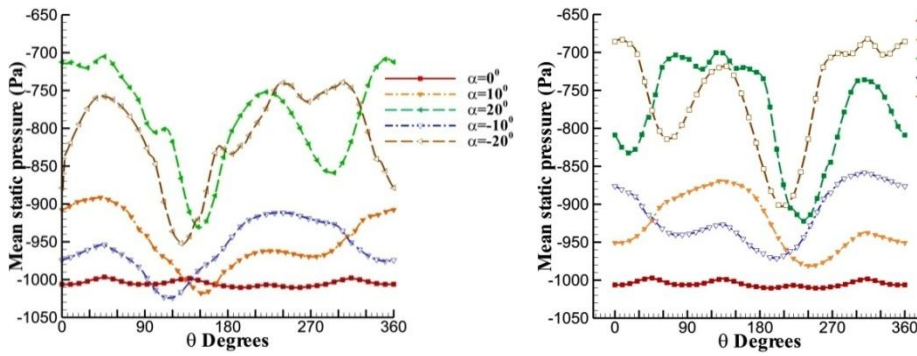


Fig. 14: Variation of mean static pressure at $x/L=0.84$ for different AoA

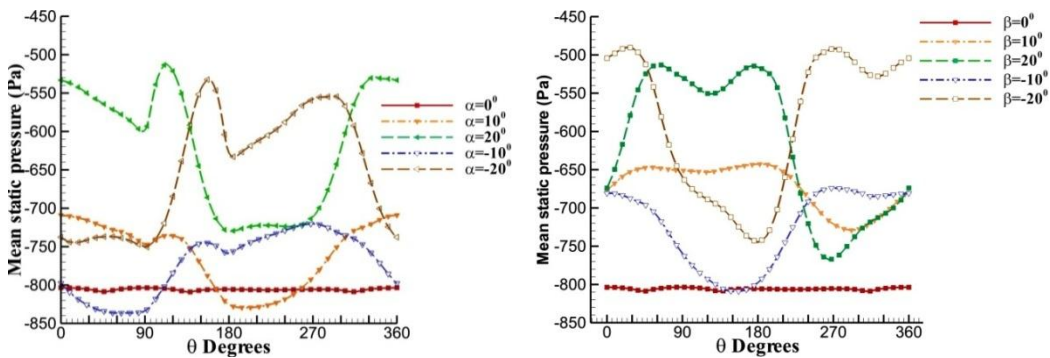


Fig 15: Variation of mean static pressure at $x/L=0.93$ for different AoA

The variation of the surface mean static pressure around the circumference of the vehicle at $x/L=0.5, 0.84$ and 0.93 for different angles of attack over Z (α) and Y (β) axes is plotted in Figs. 13, 14 and 15 respectively. At $x/L=0.5$, for 0° angle of attack, there is almost negligible variation in the pressure value. The flow is symmetric around the vehicle and is two dimensional. At $x/L=0.84$, for the same angle of attack, minor variations in the pressure value is observed. These variations in the pressure values at 0° angle of attack are due to presence of the control surface upstream of this x/L location. As we move further downstream, at $x/L=0.93$, these minor variations are subsided and the flow regains the two dimensionality and symmetric behavior. Further, for a 0° angle of attack, the maximum and the minimum values of pressure magnitude can be observed in a plane between two control surfaces.

As the angle of attack is increased, large variations in the pressure magnitude is observed at $x/L=0.5$. From Fig. 13, it is observed that even at different angles of attack, a general trend in the pressure variation at $x/L=0.5$ can be seen. As the angle of attack is increased on either side of the horizontal position (0°), either over Z-axis or Y-axis, the maximum variation in the pressure magnitude for a given angle of attack increases as the angle of attack increases. At $x/L=0.5$, irrespective of the angle of attack and irrespective of the axis, the pressure peaks and the pressure valley always lie in a plane between two control surfaces, i.e., either between 0° and 90° or 90° and 180° or 180° and 270° . For an angle of attack over Z-axis (α), whether the angle of attack is on the positive or the negative side of the horizontal ($\alpha=0^\circ$), pressure peak lies in a plane between 0° to 90° and between 180° to 270° and pressure valley lies in a plane between 90° to 180° and 270° to 360° . But, for an AoA over Y-axis, the pressure peak lies in between 270° to 360° and the pressure valley lies in between 90° to 180° for positive angles. For negative angle of attack, the peak lies between 90° to 180° and the valley between 270° to 360° . For high drift angle over the Y-axis, i.e., $\beta=20^\circ$ or $\beta=-20^\circ$, a minor pressure recovery can be observed near the minimum pressure value for that angle of attack. In general, it can be argued that the pressure variation at $x/L=0.5$, is only because of the angle of attack. It implies that the non-linearity in the flow is solely an effect due to the angle of attack. Downstream of the control surfaces, this may not be the case.

At $x/L=0.84$, the general trend in the pressure variation observed at $x/L=0.5$, totally disappeared for both α and β . The maximum pressure variation at mid-length of the vehicle is 320 Pa for α and 600 Pa for β , both for the maximum angle of attack, i.e., either 20° or -20° . But at $x/L=0.84$, the maximum pressure variation is only 300

Pa. Further, for a given angle of attack at $x/L=0.5$ and $x/L=0.84$, the difference in the maximum and minimum pressure values is found to be smaller at $x/L=0.84$. This can be attributed to a strong cross flow component of flow developed because of the presence of the control surfaces combined with the angle of attack. For 0° angle of attack, though there is a variation in the pressure around the circumference of the vehicle, the variations are very small.

Comparing Figs.13 and 15, from the pressure values, it is observed that the flow accelerates for the same angle of attack. The continuous change in the profile of the vehicle and the reducing cross section results enhanced non-linearity and greater mixing of the flow. In addition, from Figs. 13, 14 and 15, it is observed that the maximum and minimum pressure values for a given angle of attack are always observed in a plane between the control surfaces both upstream and downstream of the control surfaces. This non-linear behaviour of the flow, the setting up of strong cross flow components and the high magnitude pressure variation around the hull of the vehicle result in high drag and lift forces.

To understand the effect of the starboard-port symmetry in the geometry of the vehicle and its effect on the flow over the vehicle at various angles of attack, static pressure variation at different Azimuthal (θ) locations along the length of the vehicle are plotted. These pressure variations provide an insight into the force variation which will help in better understanding of the results presented in Table 5.

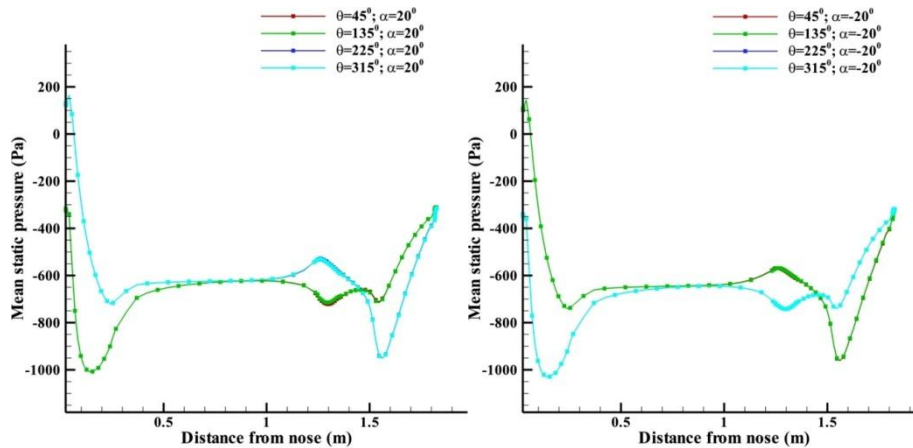


Fig. 16: Variation of mean static pressure along the length of the vehicle at various Azimuthal locations for (a) $\alpha=20^\circ$ (b) $\alpha=-20^\circ$

In Fig. 16, the variation of mean static pressure along the length of the vehicle at four different azimuthal locations for $\alpha=20^\circ$ and $\alpha=-20^\circ$ is plotted. For $\alpha=20^\circ$, it is observed that the pressure variation at $\theta=45^\circ$ and 135° is same and at $\theta=225^\circ$ and 315° is same. The same phenomenon can be observed for $\alpha=-20^\circ$ also. But, comparing $\alpha=20^\circ$ and $\alpha=-20^\circ$, it can be seen that the pressure variation at $\theta=315^\circ$ for $\alpha=20^\circ$ and $\theta=45^\circ$ for $\alpha=-20^\circ$ is almost the same.

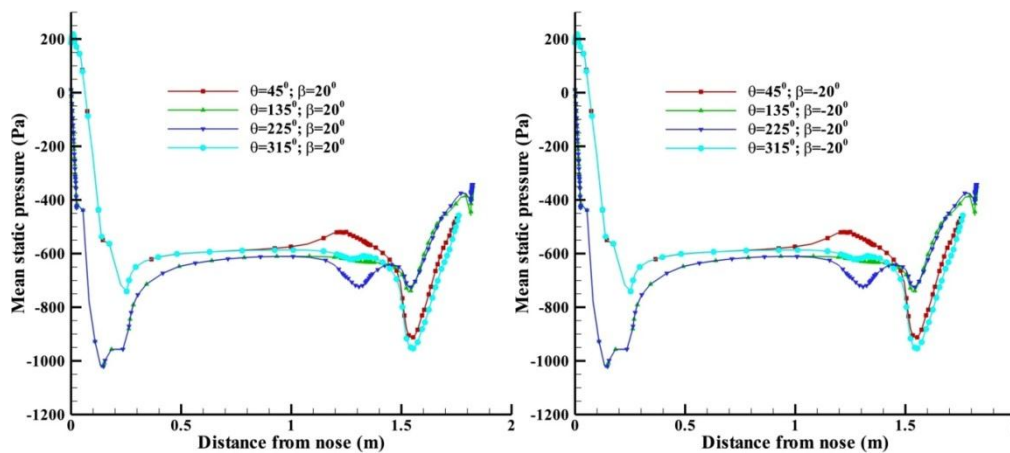


Fig. 17: Variation of mean static pressure along the length of the vehicle at various Azimuthal locations for (a) $\beta=20^\circ$ (b) $\beta=-20^\circ$

In Fig. 17, the pressure variation for $\beta=20^\circ$ and $\beta=-20^\circ$ is plotted. From Fig. 17, it is observed that the pressure variation is the same for $\theta=45^\circ$, $\theta=315^\circ$ and $\theta=135^\circ$, $\theta=315^\circ$ for both $\beta=20^\circ$ and $\beta=-20^\circ$. Though the pressure variation is the same at the specified locations, considerable deviation is observed at the location corresponding to the start of the control surfaces. Moreover, it is observed that the pressure variation at a given Azimuthal location for $\beta=20^\circ$ and $\beta=-20^\circ$ is also the same. From Figs. 16 and 17, the effect of the starboard-port symmetry in the geometry of the vehicle over the flow features is understood. For an angle of attack over Z-axis, the flow is not symmetric over the plane of symmetry, whereas, for an angle of attack over Y-axis, the flow is symmetric over the plane of symmetry along the length of the vehicle. In addition, the flow remains the same for an equal angle of rotation from null position over Y-axis which is not the case for rotation over Z-axis.

4.4 Velocity profiles

The boundary layer velocity profile is plotted between normalized streamwise velocity (U/U_∞) and normalized radial distance ($(R-R_0)/R_{\max}$), where R is the distance of a point above the hull surface, R_0 is the radius of the hull at the given streamwise location and R_{\max} is the maximum radius of the hull. The profiles are plotted at seven different x/L locations along the length of the vehicle at two different azimuthal locations, $\theta=0^\circ$ and $\theta=180^\circ$. The profiles are plotted for -20° , -10° , 0° , 10° and 20° angle of attack over both Z-axis (α) and Y-axis (β). These velocity profiles provide an insight into the flow evolution along the length of the vehicle at different azimuthal locations for different angles of attack.

From Fig. 18a, for $\alpha=\beta=0^\circ$, the normalized velocity reaches a value of unity when the normalized distance approaches 1.5. The flow accelerates at stations $x/L=0.062$, 0.125 and 0.84. The first two sections are at the middle of the nose and the end of the nose section respectively and the last section mentioned is the start of the tail section. At these three sections, the profile of the vehicle is changing because of which the flow accelerates and hence the value of the normalized velocity is more than 1. However, for $x/L=0.93$, the slope of the velocity gradient is much shallower which implies the thickening of the boundary layer. Comparing the boundary layer profiles for $\alpha=-20^\circ$ and 20° and $\alpha=-10^\circ$ and 10° , it is concluded that the flow development at the azimuthal location considered is not the same. As the angle of attack is increased on the negative side from the horizontal position, i.e., -10° and -20° , the boundary layer thickness at the mid-tail section increases which is evident from the slope of the curve for that particular section. For $\alpha=-10^\circ$ and -20° , the acceleration in the flow is higher at $x/L=0.062$ and $x/L=0.125$ when compared to $\alpha=10^\circ$ and 20° at the same streamwise location. At $x/L=0.069$, the flow accelerates for $\alpha=10^\circ$ and 20° , whereas, no such acceleration can be seen in case of $\beta=-10^\circ$ and -20° at the same x/L location. Depending on the angle of attack, the boundary layer thickness at $x/L=0.93$ is also influenced as is observed from Fig. 18. For an angle of attack on the positive side of the horizontal, i.e., 10° or 20° , the boundary layer at the mid-tail section increases with increase in the angle of attack. Whereas on the negative side, i.e., -10° or -20° , the thickness of the boundary layer at the same section reduces as is observed in Fig. 16.

Furthermore, comparing the velocity profiles for the same angle of attack over Z and Y axes respectively, it is seen that the boundary layer thickness at any given streamwise location is much higher for an angle of attack over Z-axis. Furthermore, as the angle of attack over Z-axis is increased on either side of the null position, the boundary layer thickness at the location $x/L=0.5$, 0.69, 0.74 and 0.84 increases with increase in the angle of attack unlike for an angle of attack over Y-axis. In addition, comparing the velocity profiles for $\alpha=20^\circ$ and $\alpha=-20^\circ$, it is noted that the velocity does not reach a value of unity even at a normalized distance of 3 for $x/L=0.5$, 0.69, 0.74 and 0.84. But the boundary layer thickness at these locations is much higher for $\alpha=20^\circ$ than for $\alpha=-20^\circ$. From these observations, it can be concluded that the flow around the vehicle is affected by the angle of attack.

When compared to an angle of attack over Z-axis, the flow evolution around the vehicle for different angles of attack over the Y-axis at the considered azimuthal location (0°), follow a much generalized trend as is observed from Fig. 18. For any given angle of attack, the flow accelerates at $x/L=0.069$, 0.125 and 0.74, due to change in the geometry shape at these sections. For 0° angle of attack, the velocity profiles at $x/L=0.69$ and 0.74 are more or less the same, indicating that there is no much change in flow between these two sections. But, for the maximum angle of attack, i.e., -20° or 20° , the flow accelerates at all the x/L stations except for the mid-tail section. Further, the growth of the boundary layer at various stations is same for the same angle of attack on either side of the 0° AoA.

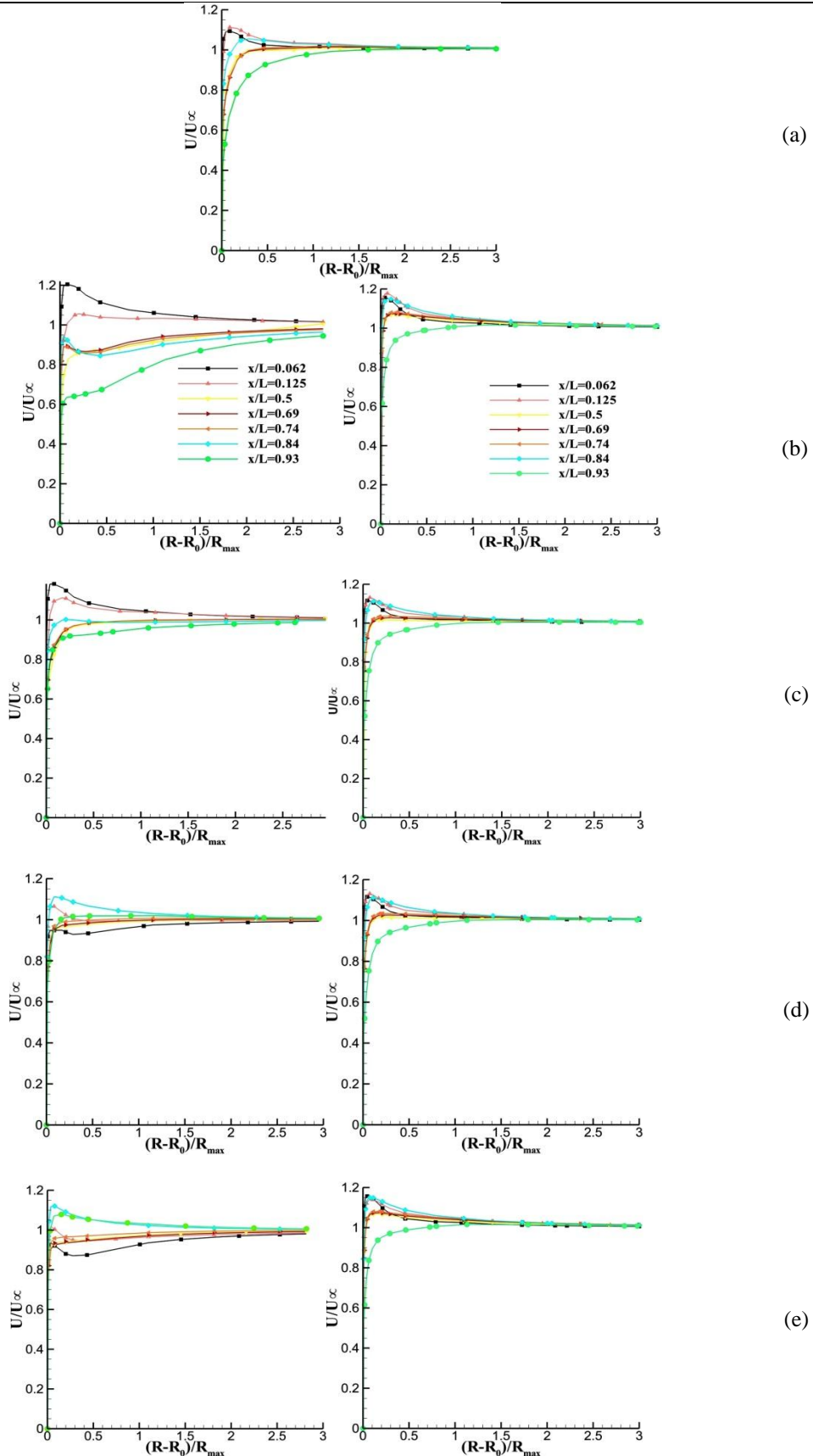


Fig. 18: Comparison of velocity profiles at $\theta=0^\circ$ for (left) $\alpha=$ (a) 0° (b) -20° (c) -10° (d) 10° (e) 20° and (right) $\beta=$ (a) 0° (b) -20° (c) -10° (d) 10° (e) 20°

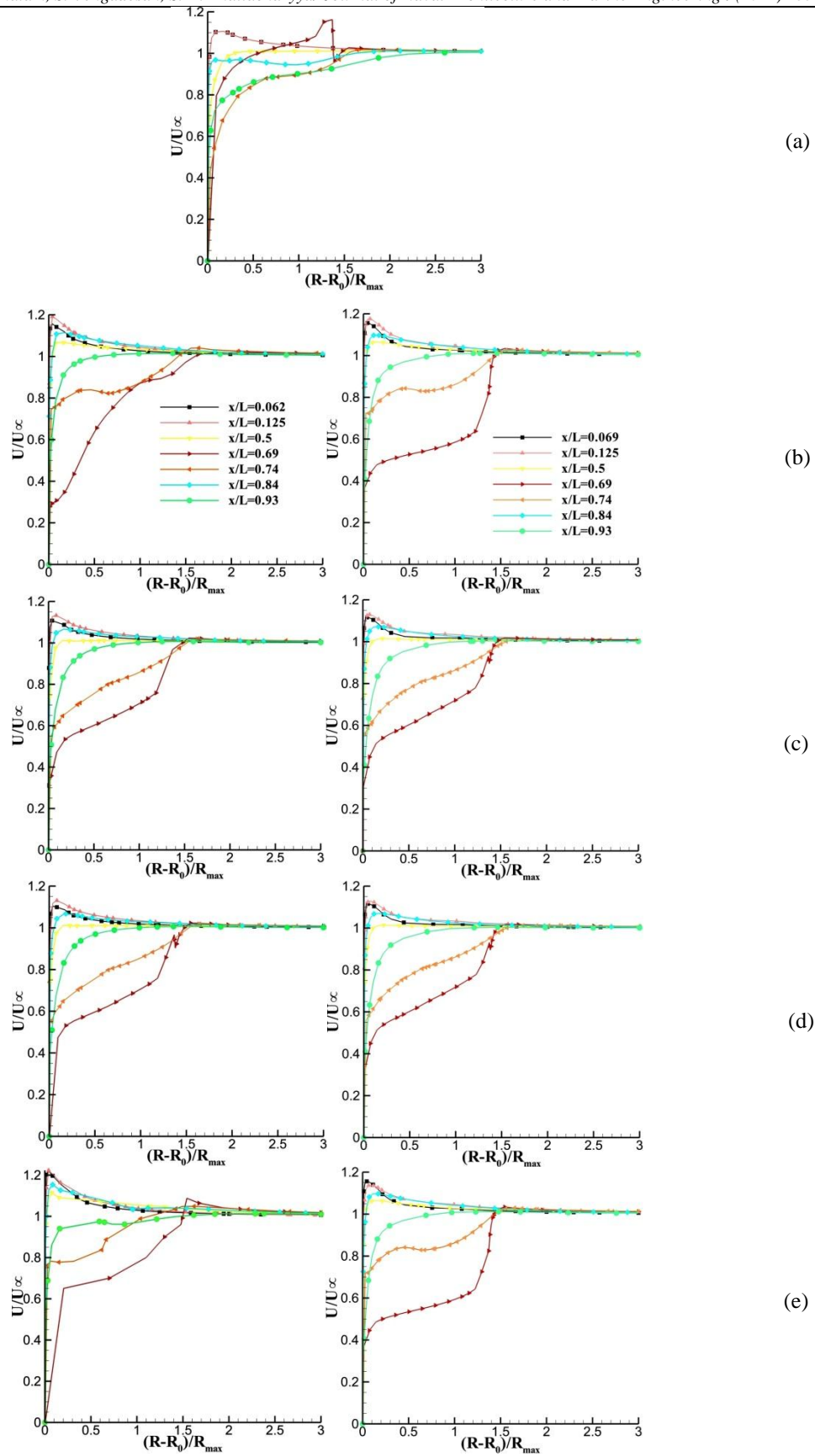


Fig. 19: Comparison of velocity profiles at $\theta=180^\circ$ for (left) $\alpha=$ (a) 0° (b) -20° (c) -10° (d) 10° (e) 20° and (right) $\beta=$ (a) 0° (b) -20° (c) -10° (d) 10° (e) 20°

Velocity profiles at $\theta=180^\circ$ are plotted in Fig. 19. A sudden, sharp drop in the mean streamwise velocity magnitude at a normalized radial distance of 1.5 for both $\alpha=0^\circ$ and $\beta=0^\circ$ at $x/L=0.69$ corresponds to the tail end of the control surface. For an angle of attack over the Z-axis, unlike at $\theta=0^\circ$, the boundary layer thickness for a given angle of attack is maximum at $x/L=0.69$, the starting section of the control surface. In addition, with an increase in the angle of attack, the boundary layer thickness at this particular section increases. The boundary layer thickness also increases at $x/L=0.74$, i.e., the location corresponding to the trailing edge of the control surface, with an increase in angle of attack. Regardless of the angle of attack, the velocity profile at all other sections almost remain the same with a small variation in the magnitude. For an angle of attack over the Y-axis, the same phenomenon can be observed as in an angle of attack over the Z-axis. But, from Fig. 19, it is observed that the velocity profiles at all the x/L locations considered are same for $-10^\circ, 10^\circ$ and $-20^\circ, 20^\circ$. Moreover at $\theta=180^\circ$, for an angle of attack over Z-axis or Y-axis, the boundary layer thickness at $x/L=0.74$ is higher for 10° or -10° than for 20° or -20° respectively. When compared to a 0° angle of attack, the boundary layer thickness at the mid-tail section is higher than that for other angles of attack. From these inferences, it is concluded that the angle of attack, combined with the presence of control surfaces, cause a non-linear component in the flow. This component of flow combined by the changing profile in the tail, results in a three dimensional flow, whose pattern remains the same but vary in the magnitude.

4.5 Pressure contours in the wake region

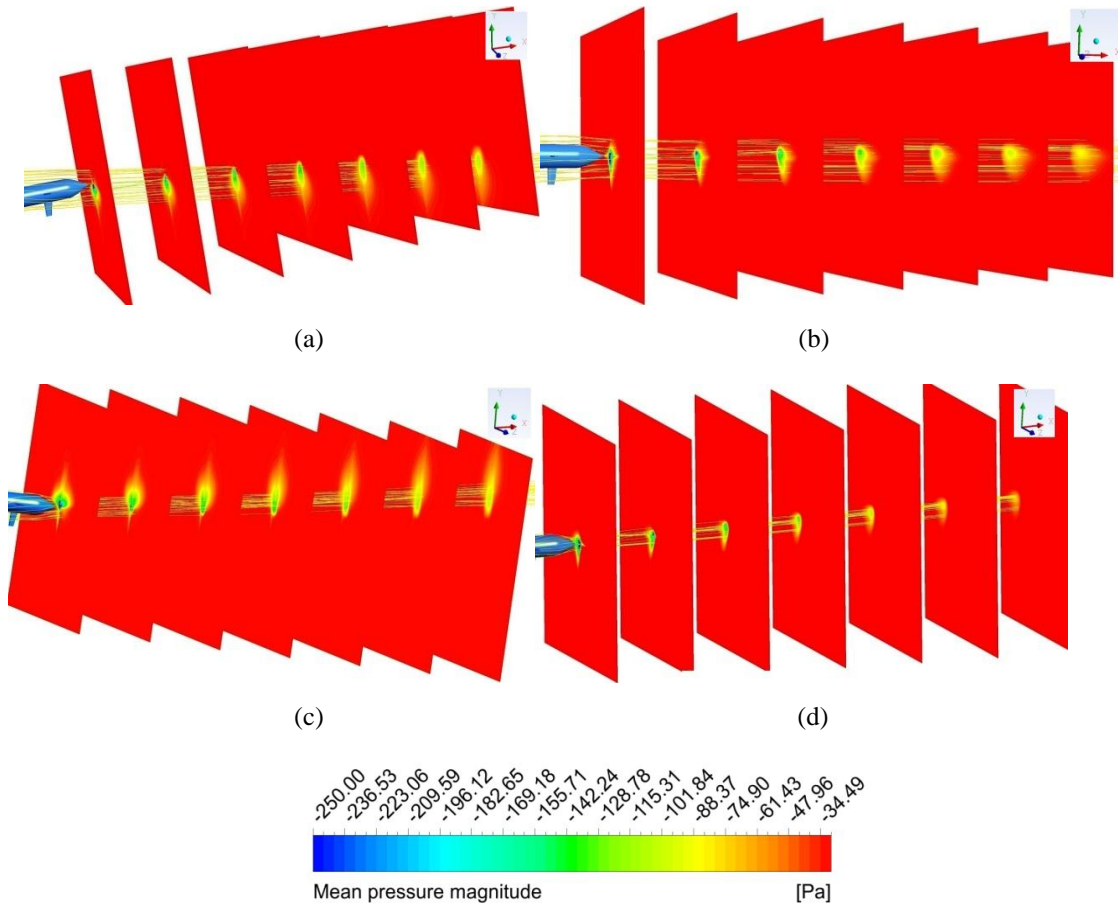


Fig. 20: Mean pressure for a) $\alpha=10^\circ$ b) $\beta=10^\circ$ c) $\alpha=-10^\circ$ d) $\beta=-10^\circ$

Mean pressure contours at various x/L locations downstream of the vehicle in planes perpendicular to the axis of angle of attack are shown in Fig. 20. Comparing the pressure contours for different angle of attack, it is observed that a low pressure region is developed immediately behind the vehicle. As the flow proceeds downstream, this low pressure region starts diffusing. It is observed that this low pressure region moves downstream in a direction opposite to the orientation of the axis of the vehicle for different AoA. The effect of the control surfaces is seen in this low pressure region. Further downstream, the low pressure region created behind the control surfaces merge. It is observed that in case of an AoA over Z-axis, the effect of the control

surface in the rudder plane is more dominant than the other two control surfaces. But, in case of an AoA over Y-axis, the effect of the control surface in the port side is dominant in case of 10^0 AoA and the one in starboard side in case of -10^0 AoA. The low pressure region in the wake of the vehicle always tends to move in a direction opposite to the orientation of the vehicle for a particular angle of attack. For example, for $\beta=10^0$, the nose of the vehicle is oriented towards the port side and the tail towards the starboard side. But, as the flow proceeds downstream, this low pressure region drifts towards the port side. Similar to the pressure distribution around the circumference of the hull, the maximum and the minimum pressure values within the low pressure region are in a plane between two control surfaces further downstream.

5. Conclusions

Systematic computational simulations are performed to understand the flow phenomena around an axisymmetric underwater vehicle with control surfaces. A validated non-linear $k-\varepsilon$ turbulence model, which performs well at higher angles of attack and which predicts and captures the non-linear flow, flow separation and reattachment is used. The three dimensional flow simulations are used to study effectively the flow pattern around an underwater vehicle at different angles of attack. Though the viscous drag remains constant, a maximum pressure drag variation of 250% is observed as the angle of attack increased from 0^0 to 20^0 or from 0^0 to -20^0 for both α and β . This variation can be attributed to the non-linear behavior of flow and flow separation and reattachment. For lower angles of attack, flow separation occurs at the tail section of the vehicle. As the angle of attack increased, this separation point moves towards the nose of the vehicle as is observed from the streamline patterns. It is also concluded that the circumferential pressure variations result in these phenomena, the pressure variation around the circumference of the vehicle at different streamwise locations is also studied. In addition, the boundary layer growth over the vehicle for different angles of attack is studied by plotting the normalized streamwise velocity against the normalized radial distance at different streamwise locations. From this study, it can be concluded that the flow around an underwater vehicle is largely affected by the angle of attack and the presence of control surfaces. In the entire study, the variation in the flow variables can be attributed to this combined effect.

References

- Alin, N., Bensow, R. E., Fureby, C., Huuva, T. and Svennberg, U. (2010): Current Capabilities of DES and LES for submarines at straight course, *Journal of Ship Research*, vol. 54, no. 3, pp. 184-196.
- Ayyappan, T., and Vengadesan, S. (2008): Three dimensional unsteady simulation of turbulent flow past a circular cylinder, *Numerical Heat Transfer- Part A (Applications)*, vol. 54, no. 2, pp. 221-234.
- Barros, E. A, Pascoal, A., and de Sa, E. (2008a): Investigation of a method for predicting AUV derivatives, *Ocean Engineering*, vol 35, pp. 1627-1636. doi: [10.1016/j.oceaneng.2008.08.008](https://doi.org/10.1016/j.oceaneng.2008.08.008)
- Barros, E. A, Pascoal, A., and de Sa. (2008b): Investigation of Normal Force and Moment Coefficients for an AUV at nonlinear angle of attack and sideslip range, *Journal of Oceanic Engineering*, vol. 33, no. 4, pp. 538-549. doi: [10.1109/JOE.2008.2004761](https://doi.org/10.1109/JOE.2008.2004761)
- Finck, R. (1978): USAF stability and DATCOM, McDonald Douglas Corporation, Global Engineering Documents.
- Jagadeesh, P., Murali, K. (2005): Application of low-Re turbulence models for flow simulation past underwater hull forms, *Journal of Naval Architecture and Marine Engineering*, vol. 2, pp. 41-54. doi: [10.3329/jname.v2i1.2029](https://doi.org/10.3329/jname.v2i1.2029)
- Kimura, I., and Hosoda, T. (2003): A nonlinear $k-\varepsilon$ model with realizability for prediction of flows around bluff bodies, *International Journal of Numerical Methods in Fluids*, vol. 42, pp. 817-837. doi: [10.1002/flid.540](https://doi.org/10.1002/flid.540)
- Madhan, R., de Sa, E., Prabhudesai, S., Sebastiao, L., Pascol, A., de Sa, E., Mascarehnas, A., Maurya, P., Navelkar, G., Afzulpurkar, S., Khalap, S. (2006): Mechanical design and development aspects of a small AUV-MAYA, 7th IFAC conference in MCMC, Lisbon.
- Myring, D. F. (1976): A theoretical study of body drag in subcritical axisymmetric flow, *Aeronautical Quarterly*, vol. 27, no. 3, pp. 186-194.
- Nahon, M. (1996): A simplified dynamics model for autonomous underwater vehicles, *Autonomous Underwater Vehicle Technology*, AUV '96, pp. 373-379.
- Newman, J. N. (1992): Panel methods in marine hydrodynamics, Keynote paper, 11th Australian Fluid Mechanics Conference.

Perrault, D., Bose, N., O'Young, S., Williams, C. D. (2003): Sensitivity of AUV response to variations in hydrodynamic parameters, *Ocean Engineering*, vol. 30, pp. 779-811. doi: [10.1016/S0029-8018\(02\)00043-4](https://doi.org/10.1016/S0029-8018(02)00043-4)

Prestero, T. (2001): Verification of a six-degree of freedom simulation model for the REMUS autonomous underwater vehicle, Master Thesis, MIT.

Ramesh, V., Vengadesan, S., Narasimhan, J.L. (2006): 3D Unsteady RANS simulation of turbulent flow over bluff body by non-linear model, *International Journal for Numerical Methods in Heat and Fluid Flow*, vol. 26, no. 6, pp. 660-673.

Sahin, I., Crane, J. W., Watson, K. P. (1997): Application of a panel method to hydrodynamics of Underwater Vehicles, *Ocean Engineering*, vol. 24, no. 6, pp. 501-512. doi: [10.1016/S0029-8018\(96\)00026-1](https://doi.org/10.1016/S0029-8018(96)00026-1)

Sakthivel, R., Vengadesan, S., Bhattacharyya, S. K. (2011): Application of non-linear k- ϵ turbulence model in simulation of flow over underwater axisymmetric hull at higher angle of attack, *Journal of Naval Architecture and Marine Engineering*, vol. 8, no. 2, pp. 147-163. doi: [10.3329/jname.v8i2.6984](https://doi.org/10.3329/jname.v8i2.6984)

Sarkar, T., Sayer, P. G., Fraser, S. M. (1997): A study of underwater vehicle hull forms using computational fluid dynamics, *International Journal for Numerical Methods in Fluids*, vol. 25, pp. 1301-1313.